Identification of material parameters for a violin bridge from dynamic output data

Sandra Marschke, Wolfgang Ring

August 14, 2020

Abstract

In this work we present an output least-squares method for the identification of elastic material parameters for orthotropic material specimens like a wooden violin bridge. The basis for the optimisation are measurements of the transient behaviour of the investigated object. Such an approach points out an alternative to the widely spread usage of destructive tensile tests. Based on the dynamical output data we then design a cost functional assessing its amplitude and phase information for the optimisation. We then derive the sensitivities of this cost functional with help of the adjoint equation and subsequently explain the algorithmic approach via a quasi-Newton method, i.e. the BFGS-method in combination with an Armijo-Goldstein line search technique. For the numerical simulations the damped elastic wave equation on the complex three-dimensional violin bridge geometry will serve as the modelling equation. In the last section we complete the discussion with an elucidation of several successful numerical experiments for the violin bridge.

1   Introduction

The aim of this work is the development of a reliable parameter identification algorithm to reconstruct the material parameters of a wood specimen from data provided by a measured transient output signal. Our main focus will be on the application of the identification process for the material parameters of a violin bridge. These parameters are very relevant to the individual vibrational behaviour of the bridge because they significantly affect the sound properties of the violin bridge, and thus the sound of the overall instrument as well. The violin bridge can be considered as the first link in a chain of mechanical wave guides which transport the vibration of the string into the acoustical space surrounding the instrument. See also [10], [1, 8] for the importance of the violin bridge from a physical point of view. An image of a typical violin bridge mounted on the instrument can be seen in Figure 1. The bridge has obviously a complex three dimensional shape and is made from maple wood which is highly anisotropic in its elastic material parameters. The elastic parameters of the wood are the Youngs moduli E_{kk}, the shear moduli G_{ij} and the Poisson's ratios ν_{kl} where $k, l \in \{1, 2, 3\}$. See Section 2.1 for further discussions and elucidation about the considered parameters. These quantities can be measured using various physical experimental setups. Classically the determination of orthotropic materials are based on tensile tests [5, 13, 14]. A good overview on the state of the art in the field of mechanical parameter testing can be found in [18]. Experiments of this kind, however, are usually destructive tests and require a sufficiently large sample of the material in a standardised geometric form. For a singular, non-reproduceable object like a violin bridge, which was, often decades ago, cut from a slap of wood, these testing methods are not applicable. In the last two decades affort has been made to determine materials in a nondestructive way by numerical optimisation. An example from biomedicine is the reconstruction of elastic properties from ultrasonic measurements like in [9, 19]. For general anisotropic medias there were many inverse problems composed to derive the anistropic material parameters from full-field displacement measurements, see e.g. [11, 3]. The measurements as well as the optimisation for this approach are very complex and computationally costly because one always needs to compare displacements over the whole surface of the object. Furthermore, the necessary measurement data are often not available in a practical setting. In contrast, the method we will present in the following chapters is based on measurements of the transient behaviour of a material specimen at a single measurement point. These measurements are technical much simpler and comparably easy to conduct. This opens our method to a wide field of potential applications where the technology of a well-equipped laboratory is not at hand. Our approach

Figure 1: Closeup of a violin bridge mounted on the instrument.

via an inverse output least squares problem, therefore, is a valuable alternative leaving the considered object unaffected during the parameter identification process.

Starting from an input-output measurement at two defined points, we analyse the transient behaviour with tools from signal processing. Doing the same in our numerical simulation, we then can compare the measured and simulated signals in the frequency domain. For this purpose we design a L^2-costfunctional comparing amplitude and phase of the two signals over a prescribed frequency interval.

The article is structured as follows: In Chapter 2 we start with the explanation of the mathematical model designed for the elastic wave equation on a domain describing the 3D violin bridge geometry. Here we discuss the dynamic state model of the elastic wave equation on the one side in Subsection 2.1, and isogeometric analysis as a methodical basis for the numerical implementations on the other side in Subsection 2.2. Afterwards, we formulate the variational form of the parameter identification problem in Chapter 3 and introduce the applied costfunctional J. Subsequently, we derive the sensitivities of J with respect to the considered material parameters in Chapter 4 with help of the adjoint equation. With the sensitivities on hand, we can turn to the parameter optimisation and its concrete algorithmic implementation in Chapter 5. The results of several numerical experiments for the parameter identification for the example of a violin bridge presented in Chapter 6 will then serve to demonstrate the abilities of the designed optimisation algorithm.

2 Mathematical Model

Before we start out with the discussion of the modelling equations for the vibrational behaviour of the violin bridge, a few comments on notation are adequate. We will deal with different types of vectors: Three dimensional vectors in physical space and (usually very high dimensional) vectors of coefficients for finite element approximations. We will denote both types using bold letters, e.g. $\mathbf{x}$ or $\mathbf{w}$. The scalar product for three-dimensional vectors is written as $\mathbf{x} \cdot \boldsymbol{\xi}$ whereas the scalar product for finite element coefficient vectors is written as $\langle \mathbf{w}, \mathbf{v} \rangle$. Moreover, we use subscripts w_j to address individual finite element coefficients but superscripts x^m to address components of three-dimensional vectors.

2.1 Dynamic state model

In order to get realistic simulation results, we need a physically and numerically accurate and reliable model for the vibrational behaviour of the violin bridge. This will make our research results valuable to practitioners as well. The underlying physical model for the small-amplitude vibrations of the violin bridge is the elastic damped wave equation on a bounded domain $\Omega \subset \mathbb{R}^3$ which is a piecewise smooth, Lipschitz continuous, not simply connected open set in $\mathbb{R}^3$. The Dirichlet boundary $\Gamma \subset \partial\Omega$ is a nonempty subset of the boundary $\partial\Omega$. On Γ we assume that the bridge is clamped and remains stationary throughout the vibrational movement after excitation, i.e. we have zero boundary conditions here. A natural choice for Γ are the two bases of the feet of

the bridge where the bridge is in contact with the top plate of the violin. The dynamic evolution usually starts from the static equilibrium, so we chose the initial conditions $\mathbf{u}(0,\mathbf{x}) = \dot{\mathbf{u}}(0,\mathbf{x}) = 0$ for $\mathbf{x} \in \Omega$. All together we get the following system equations:

$$
\begin{aligned}
\rho\ddot{\mathbf{u}}(t,\mathbf{x}) + d(\dot{\mathbf{u}}(t,\mathbf{x})) - \nabla \cdot \boldsymbol{\sigma}(\mathbf{u}(t,\mathbf{x})) &= \mathbf{f}(t,\mathbf{x}), \quad t \in [0,T], \ \mathbf{x} \in \Omega, \\
\mathbf{u}(0,\mathbf{x}) = \dot{\mathbf{u}}(0,\mathbf{x}) &= 0 & \mathbf{x} \in \Omega, \\
\mathbf{u}(t,\mathbf{x}) &= 0 & t \in [0,T], \ \mathbf{x} \in \Gamma
\end{aligned}
\tag{1}
$$

with given right hand side $\mathbf{f} \in L^2([0,T]; H^1(\Omega)^*)$. The function $\mathbf{f}$ describes the excitation. It is usually either a short pulse or a chirp signal acting on some point $\mathbf{x}_{\text{in}} \in \partial\Omega\backslash\Gamma$. Also the damping term in (1) needs further specification. In our case we apply Rayleigh damping (see [12, Section 3.7.2]) and thus the damping term takes the form

$$
d(\dot{\mathbf{u}}(t,\mathbf{x})) := \alpha_M \dot{\mathbf{u}}(t,\mathbf{x}) + \alpha_K \frac{d}{dt}\left[\nabla \cdot \boldsymbol{\sigma}\big(\mathbf{u}(t,\mathbf{x})\big)\right].
\tag{2}
$$

The Rayleigh damping thus models the acting damping forces as a linear combination of one factor which is proportional to velocity and a second factor which is proportional to the rate of change of the local elastic energy.

To clarify the notations of linear elasticity we take a look at the strong form of (1):

$$
\rho\ddot{\mathbf{u}} = \boldsymbol{\nabla} \cdot \boldsymbol{\sigma} + \mathbf{f} + \big(\alpha_K \boldsymbol{\nabla} \cdot \dot{\boldsymbol{\sigma}} - \alpha_M \dot{\mathbf{u}}\big)
\tag{3a}
$$

together with the constitutive equation (Hook's law)

$$
\boldsymbol{\sigma} = \mathbb{C} : \boldsymbol{\varepsilon}(\mathbf{u})
\tag{3b}
$$

for the stress tensor $\boldsymbol{\sigma}$ and the strain $\boldsymbol{\varepsilon}(\mathbf{u}) = \frac{1}{2}\big(\nabla\mathbf{u} + \nabla\mathbf{u}^\top\big)$. The Cauchy strain tensor $\boldsymbol{\varepsilon}(\mathbf{u}) = \frac{1}{2}\big(\nabla\mathbf{u} + \nabla\mathbf{u}^\top\big)$, therefore, is linearly connected to the Cauchy stress tensor $\boldsymbol{\sigma}(\mathbf{u})$ via the constitutive relation $\boldsymbol{\sigma}(\mathbf{u}) = C : \boldsymbol{\varepsilon}(\mathbf{u})$, where $C = C_{ijkl}$ is a fourth order tensor. For our applications we model the maple wood of the bridge as a homogeneous orthotropic material. Under this assumption, we can employ various symmetry properties and arrive at the following matrix form of the constitutive relation

$$
\begin{pmatrix} \sigma_{11} \\ \sigma_{22} \\ \sigma_{33} \\ \sigma_{23} \\ \sigma_{31} \\ \sigma_{12} \end{pmatrix} = \begin{pmatrix} C_{11} & C_{12} & C_{13} & 0 & 0 & 0 \\ C_{12} & C_{22} & C_{23} & 0 & 0 & 0 \\ C_{13} & C_{23} & C_{33} & 0 & 0 & 0 \\ 0 & 0 & 0 & C_{44} & 0 & 0 \\ 0 & 0 & 0 & 0 & C_{55} & 0 \\ 0 & 0 & 0 & 0 & 0 & C_{66} \end{pmatrix} \cdot \begin{pmatrix} \varepsilon_{11} \\ \varepsilon_{22} \\ \varepsilon_{33} \\ \varepsilon_{23} \\ \varepsilon_{31} \\ \varepsilon_{12} \end{pmatrix}
\tag{4}
$$

for $\sigma_{ij} = \big(\boldsymbol{\sigma}(\mathbf{u})\big)_{ij}$ and $\varepsilon_{ij} = \big(\boldsymbol{\varepsilon}(\mathbf{u})\big)_{ij}$, $i,j = 1,2,3$ (see [17, Section 2.4] for details). Equation (4) can be written in the compact form

$$
\underline{\boldsymbol{\sigma}} = M_C \, \underline{\boldsymbol{\varepsilon}}
\tag{5}
$$

with the sparsity structure of M_C given in (4). In the engineering literature it is usual to designate the coefficients of the inverse matrix $m_C = (M_C)^{-1}$. In this setting one works with the matrix

$$
m_C = \begin{pmatrix} \frac{1}{E_{11}} & -\frac{\nu_{21}}{E_{22}} & -\frac{\nu_{31}}{E_{33}} & 0 & 0 & 0 \\ -\frac{\nu_{12}}{E_{11}} & \frac{1}{E_{22}} & -\frac{\nu_{32}}{E_{33}} & 0 & 0 & 0 \\ -\frac{\nu_{13}}{E_{11}} & -\frac{\nu_{23}}{E_{22}} & \frac{1}{E_{33}} & 0 & 0 & 0 \\ 0 & 0 & 0 & \frac{1}{G_{23}} & 0 & 0 \\ 0 & 0 & 0 & 0 & \frac{1}{G_{13}} & 0 \\ 0 & 0 & 0 & 0 & 0 & \frac{1}{G_{12}} \end{pmatrix}.
$$

This matrix is determined by the Young's moduli E_{kk}, the Poisson rations ν_{kl} and the shear moduli G_{kl} of the orthotropic material.

In preperation of the finite element formulation in the following section, we write (3a) in its weak form:

$$
\int_\Omega \rho\langle\boldsymbol{\varphi},\ddot{\mathbf{u}}\rangle\,d\mathbf{x} + \int_\Omega \Big(\alpha_M\langle\boldsymbol{\varphi},\dot{\mathbf{u}}\rangle + \alpha_K\boldsymbol{\varepsilon}(\boldsymbol{\varphi}) : \big(\mathbb{C}\,\boldsymbol{\varepsilon}(\dot{\mathbf{u}})\big)\Big)\,d\mathbf{x}
\tag{6}
$$

$$
+ \int_\Omega \boldsymbol{\varepsilon}(\boldsymbol{\varphi}) : \big(\mathbb{C}\,\boldsymbol{\varepsilon}(\mathbf{u})\big)\,d\mathbf{x} = \big\langle\boldsymbol{\varphi},\mathbf{f}\big\rangle_{\big(\mathbf{H}^1_\Gamma(\Omega),(\mathbf{H}^1_\Gamma)*(\Omega)\big)}
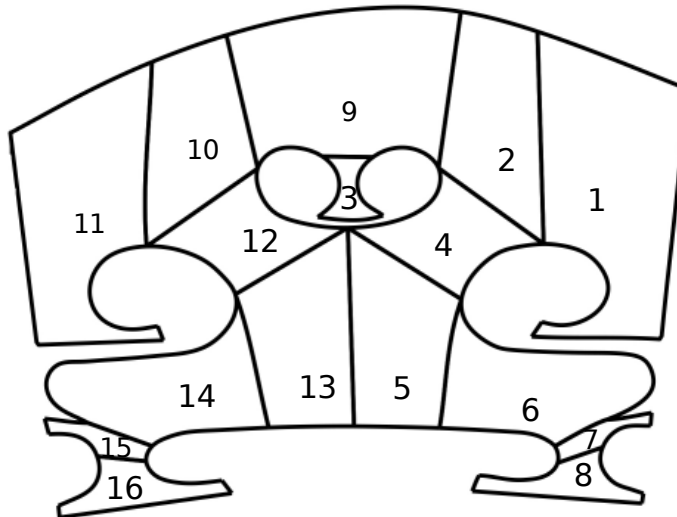\tag{7}
$$

3

Figure 2: Sketch of the decomposition of the bridge into individual patches for NURBS discretisation.

for all $\boldsymbol{\varphi} \in \mathbf{H}_\Gamma^1(\Omega)$. Here we use the Sobolev spaces

$$\mathbf{H}_\Gamma^1(\Omega) = \mathbf{H}_\Gamma^1(\Omega; \mathbb{R}^3) = \{\mathbf{u} : \Omega \to \mathbb{R}^3 \, : \, u_i \in H^1(\Omega) \text{ for } i = 1, 2, 3 \text{ and } \mathbf{u}|_\Gamma = 0\}$$

and its corresponding dual space $(\mathbf{H}_\Gamma^1)^*(\Omega)$ and almost every $t \in [0, T]$. The second integral in (6) describes the Rayleigh damping mechanism employed in the model.

2.2 Numerical methods and finite element formulation

The numerical solution of the wave equation (6) requires sophisticated discretisation techniques if reliable numerical simulations shall be achieved. Here the main difficulty is the complex geometrical shape of the domain Ω. To pay respect to this, we chose isogeometric elements both, for the description of the geometry, and for the finite element basis. We do this by decomposing Ω into a number of patches, each of it being homeomorphic to the unit cube in $\mathbb{R}^3$ where the homeomorphism is parametrised using tensor products of non-uniform rational B-splines (NURBS). On each patch a local NURBS finite-element basis is defined. The interaction between the different patches is resolved introducing mortar elements on the common interface between two patches which act as Lagrange multipliers ensuring regularity of the global solution across the interface. (See [7] and [4] for details regarding theory and implementation.) In Figure 2.2 a schematic drawing of a bridge shows the chosen decomposition into patches where each patch is the homeomorphic image of the unit cube in $\mathbb{R}^3$ under a NURBS-based bijective transformation. Note (especially in patches No. 1, 9 and 11) that corners and edges present in the patch need not necessarily be the images of corners and edges of the unit cube under the NURBS transformation. In fact kinks and corners can be realised using NURBS by decreasing the regularity of the rational B-spline basis locally. In the derivation of the FE-model for the violin bridge, we constructed a highly precise NURBS geometry from measured μ-CT scan data of an actual bridge. A detailed explanation of this process can be found in [15].

To solve (6) numericaly we approximate the solution by a linear combination of NURBS basis functions N_j with time-dependent three dimensional coefficient vector $\mathbf{y}_j(t) = \left(y_j^1(t), y_j^2(t), y_j^3(t)\right)^t$:

$$\mathbf{u}(t, \mathbf{x}) = \sum_{j=1}^N N_j(\mathbf{x}) \, \mathbf{y}_j(t) \, . \tag{8}$$

The patchwise defined isogeometric basis functions $N_j : \Omega \to \mathbb{R}$ form a NURBS basis $\hat{\mathbf{N}} = \{N_j : \quad j = 1, ..., N\}$, N being the number of basis function on all individual patches. We assemble the individual coefficient vectors $\mathbf{y}_j$ into an overall state vector $\mathbf{y}(t)$. Evaluating the weak form of the elastic wave equation for all test functions $\boldsymbol{\varphi}_j^m(\mathbf{x}) = N_j(\mathbf{x}) \, \mathbf{e}^m$, with $\mathbf{e}^m$, $m = 1, 2, 3$, denoting the canonical basis in $\mathbb{R}^3$, gives the discrete approximation

4

of (6) which takes the form of a second order ODE-system for the coefficient vector $\mathbf{y}(t)$:

$$M\mathbf{y}''(t) + D\mathbf{y}'(t) + A\mathbf{y}(t) = \mathbf{f}(t), \tag{9a}$$

$$\mathbf{y}(0) = \mathbf{y}'(0) = 0. \tag{9b}$$

The mass matrix M is build up from the 3×3 sub-matricies $(M_{ij}^{mn})_{m,n=1}^3$ with $M_{ij}^{mn} = \rho \int_\Omega N_i(\mathbf{x}) N_j(\mathbf{x}) \delta_{mn} d\mathbf{x}$. The stiffness matrix A contains the sub-matrices $A_{ij} = \int_\Omega \varepsilon(\mathbf{N}_i(\mathbf{x})) : (\mathbb{C}\,\varepsilon(\mathbf{N}_j(\mathbf{x}))) d\mathbf{x}$ and the damping matrix D contains the entries $D_{ij} = \alpha_M M_{ij} + \alpha_K A_{ij}$. Here $\mathbf{N}_j(\mathbf{x}) = \sum_{m=1}^3 N_j(\mathbf{x})\mathbf{e}^m = \sum_{m=1}^3 \boldsymbol{\varphi}_j^m(\mathbf{x})$ is the vector valued version of the basis function $N_j(\mathbf{x})$. The force vector $\mathbf{f}(t)$ on the right-hand side comprises the forcing terms $\langle \boldsymbol{\varphi}_i^m, \mathbf{f}(t) \rangle_{\mathbf{H}_\Gamma^1,(\mathbf{H}_\Gamma^1)*}$. We choose a time-dependent point source of the form

$$\left\langle \boldsymbol{\varphi}_i^m, \mathbf{f}(t) \right\rangle_{\mathbf{H}_\Gamma^1,(\mathbf{H}_\Gamma^1)*} = f(t)\,\boldsymbol{\varphi}_i^m(\mathbf{x}_{\mathrm{in}}) \tag{10}$$

with a given input signal $f : [0, T] \to \mathbb{R}$, usually a chirp signal at some fixed input location $\mathbf{x}_{\mathrm{in}} \in \partial\Omega$. The elastic material parameters E_{kk}, ν_{kl} and G_{kl} occur in the stiffness matrix A and hence also in the damping matrix D. If we define the parameter vector $\mathbf{p}$ as

$$\mathbf{p} = \left(E_{11}, E_{22}, E_{33}, \nu_{21}, \nu_{31}, \nu_{32}, G_{23}, G_{13}, G_{12} \right)^\top \tag{11}$$

then all finite element matrices are $\mathbf{p}$-dependent. We usually write $M(\mathbf{p})$, $D(\mathbf{p})$ and $A(\mathbf{p})$. If certain of the parameters are set to fixed values and thus will be removed from the list of estimated parameters, corresponding $\mathbf{p}$-dependencies might disappear.

3   Variational formulation of the parameter identification problem

We now address the problem of identifying the physical parameters from measured input-output behavior of the considered physical system and introduce a cost functional to reach his aim in an iterative optimisation process. As mentioned in section 2.1 we use just one fixed input signal acting at a given point $\mathbf{x}_{\mathrm{in}}$ on the surface of the bridge.

The three-dimensional output data are given as

$$\mathbf{u}_{\mathrm{out}}(t) = \sum_{m=1}^3 u_{\mathrm{out}}^m(t)\,\mathbf{e}^m = \sum_{j=1}^N N_j(\mathbf{x}_{\mathrm{out}})\,\mathbf{y}_j(t) \tag{12}$$

for a given fixed measurement point $\mathbf{x}_{\mathrm{out}} \in \partial\Omega$, $\mathbf{x}_{\mathrm{out}} \neq \mathbf{x}_{\mathrm{in}}$. The time interval $[0, T]$ on which the output signal is active will be finite. We shall, however, assume that T is large and the damping strong enough such that all relevant signals have faded out at the final time $t = T$. It will be convenient to extend the signals by zero onto $[0, \infty)$ especially when dealing with Fourier transforms. If the amplitude decay at the end of the time-interval is strong enough this extension procedure will not introduce spurious frequencies in the Fourier transforms of the signals.

To solve the parameter estimation problem, comparing measured and simulated outputs directly in an output-least squares formulation turns out to be unfeasible. Due to the oscillatory nature of the output signal, the resulting optimisation problem has many spurious solutions (local minima of the cost functional) and the identification algorithm is very likely to get stuck in one of these minimas. Instead, we fit the output signal to the measured signal in frequency space, where we choose the fitting terms for amplitude and phase independently. For the amplitude fitting we define a Kullback-Leibler type cost functional in the form

$$J_{\mathrm{am}}(\mathbf{p}) = \sum_{m=1}^3 \int_{\omega_{\mathrm{min}}}^{\omega_{\mathrm{max}}} \left(\log \frac{|\hat{u}_{\mathrm{out}}^m(\omega)| + \varepsilon}{|\hat{u}_{\mathrm{dat}}^m(\omega)| + \varepsilon} \right)^2 d\omega. \tag{13}$$

We hence compare amplitudes of output- and measured data in frequency domain in a logarithmic scale. The other term in the cost functional is a least-squares data fit of the phases. It reads

$$J_{\mathrm{ph}}(\mathbf{p}) = \sum_{m=1}^3 \int_{\omega_{\mathrm{min}}}^{\omega_{\mathrm{max}}} \left(\frac{\hat{u}_{\mathrm{out}}^m}{|\hat{u}_{\mathrm{out}}^m| + \varepsilon} - \frac{\hat{u}_{\mathrm{dat}}^m}{|\hat{u}_{\mathrm{dat}}^m| + \varepsilon} \right)^2 d\omega. \tag{14}$$

In both cases $\hat{u}(\omega)$ denotes the Fourier transform for a given signal $u : [0, \infty) \to \mathbb{R}$:

$$\hat{u}(\omega) = \int_0^\infty e^{-2\pi i \omega t}\, u(t)\, dt\,.$$

The frequency interval $I_\omega = [\omega_{\min}, \omega_{\max}]$ for the data fit is chosen such that frequency values which are relevant for the the acoustical properties lie within I_ω but the dominant frequencies in the data noise are cut off. The role of the non-degeneracy parameter $\varepsilon > 0$, especially in equation (13), will be discussed in detail later in Chapter 5.

For the identification of the parameter vector $\mathbf{p}$ from the given measured data u_{dat} we minimise the combined cost functional

$$J(\mathbf{p}) = J_{\mathrm{am}}(\mathbf{p}) + J_{\mathrm{ph}}(\mathbf{p}) \tag{15}$$

over a set $\mathbf{P} \subset \mathbb{R}^9$ of physically feasible parameter vectors . Note that both data-fit terms (13) and (14) depend on the parameter $\mathbf{p}$ only indirectly via the solution $\mathbf{y}(t, \mathbf{p})$ of the discrete state equation (9) and consequently via the output signal $\mathbf{u}_{\mathrm{out}}(t, \mathbf{p})$ where the actual $\mathbf{p}$-dependence lies in the coefficients of the system matrices for (9). Denoting

$$\tilde{J}_{\mathrm{am}}(\mathbf{u}) = \sum_{m=1}^3 \int_{\omega_{\min}}^{\omega_{\max}} \left(\log \frac{|\hat{u}_{\mathrm{out}}^m(\omega)| + \varepsilon}{|\hat{u}_{\mathrm{dat}}^m(\omega)| + \varepsilon} \right)^2 d\omega$$

and

$$\tilde{J}_{\mathrm{ph}}(\mathbf{u}) = \sum_{m=1}^3 \int_{\omega_{\min}}^{\omega_{\max}} \left(\frac{\hat{u}_{\mathrm{out}}^m}{|\hat{u}^m| + \varepsilon} - \frac{\hat{u}_{\mathrm{dat}}^m}{|\hat{u}_{\mathrm{dat}}^m| + \varepsilon} \right)^2 d\omega$$

for a given vector-valued signal $\mathbf{u} : [0, \infty) \to \mathbb{R}$, we have

$$J_{\mathrm{am}}(\mathbf{p}) = \tilde{J}_{\mathrm{am}}(\mathbf{u}_{\mathrm{out}}(\mathbf{p})) \text{ and } J_{\mathrm{ph}}(\mathbf{p}) = \tilde{J}_{\mathrm{ph}}(\mathbf{u}_{\mathrm{out}}(\mathbf{p})).$$

For later reference we define the data mismatch in the amplitude part of the cost functional (13) as

$$\mathcal{J}_{\mathrm{am}}(\omega; \mathbf{p}, \varepsilon) = \sum_{m=1}^3 \left(\log \frac{|\hat{u}_{\mathrm{out}}^m(\omega)| + \varepsilon}{|\hat{u}_{\mathrm{dat}}^m(\omega)| + \varepsilon} \right)^2. \tag{16}$$

4 Sensitivity analysis and adjoint equation

In this section we will compute the sensitivities with respect to the introduced cost functional (15). Since the explicit computation via the forward problem would be computationally very costly we therefore chose to compute them via an adjoint approach. First we give an abstract description of the set of feasible set parameters by $\mathbf{P} = \{\mathbf{p} \in \mathbb{R}^9 : \mathbf{p}_{\mathrm{lb}} \leqslant \mathbf{p} \leqslant \mathbf{p}_{\mathrm{ub}}\}$ with given vectors $\mathbf{p}_{\mathrm{lb}} \in \mathbb{R}^9_{>0}$ and $\mathbf{p}_{\mathrm{ub}} \in \mathbb{R}^9_{>0}$ of upper and lower bounds for the parameters. Using standard regularity results for linear ODEs (c.f. Amann [2, Theorem 9.2]) it follows that $\mathbf{p} \mapsto \mathbf{y}(\cdot)$ is a mapping in $\mathcal{C}^1\big(\mathbf{P}, \mathcal{C}^1([0, T], \mathbb{R}^d)\big)$ on the set $\mathbf{P}$, where d is the total number of degrees of freedom in (9). Moreover, the partial derivative $\mathbf{y}_{p_\nu}$ with respect to parameter p_ν, $\nu = 1, 2, \ldots, 9$ solves the sensitivity equation

$$M\mathbf{y}_{p_\nu}''(t) + D\mathbf{y}_{p_\nu}' + A\mathbf{y}_{p_\nu}(t) = -M_{p_\nu}\mathbf{y}''(t) - D_{p_\nu}\mathbf{y}'(t) - A_{p_\nu}\mathbf{y}(t) \text{ on } [0, T], \tag{17a}$$

$$\mathbf{y}_{p_\nu}(0) = \mathbf{y}_{p_\nu}'(0) = 0 \tag{17b}$$

for $\nu = 1, 2 \ldots, 12$. Here $\mathbf{y} = \mathbf{y}(t, \mathbf{p})$ is the solution to the discrete state equation (9) for the given parameter vector $\mathbf{p}$. Moreover, we assume that the right-hand side of (9) is independent of the parameter $\mathbf{p}$. Using (12) for the representation of $\mathbf{u}_{\mathrm{out}}$, it is obvious that also the output signal $\mathbf{u}_{\mathrm{out}}$ is of the same differentiability class as $\mathbf{y}(t)$ and we have

$$\mathbf{u}_{\mathrm{out}, p_\nu}(t) = \sum_{j=1}^N N_j(\mathbf{x}_{\mathrm{out}})\, \mathbf{y}_{j, p_\nu}(t)\,.$$

Applying this formulation for $\mathbf{u}_{\mathrm{out}, p_\nu}(t)$ we get the following expression for the derivatives of J_{am} and J_{ph} with respect to the parameter p_ν:

$$J_{\mathrm{am}, p_\nu}(\mathbf{p}) = \tilde{J}_{\mathrm{am}, \mathbf{u}}(\mathbf{u}_{\mathrm{out}}(\mathbf{p})) \cdot \mathbf{u}_{\mathrm{out}, p_\nu}(\mathbf{p}) \text{ and } J_{\mathrm{ph}, p_\nu}(\mathbf{p}) = \tilde{J}_{\mathrm{ph}, \mathbf{u}}(\mathbf{u}_{\mathrm{out}}(\mathbf{p})) \cdot \mathbf{u}_{\mathrm{out}, p_\nu}(\mathbf{p}) \tag{18}$$

where

$$\tilde{J}_{\mathrm{am},\mathbf{u}}(\mathbf{u}) \cdot \mathbf{v} = 4 \sum_{m=1}^{3} \int_{\omega_{\min}}^{\omega_{\max}} \log\left(\frac{|\hat{u}^m| + \varepsilon}{|\hat{u}_{\mathrm{dat}}^m| + \varepsilon} \right) \frac{\mathrm{Re}\left(\hat{u}^m\, \overline{\hat{v}^m} \right)}{\left(|\hat{u}^m| + \varepsilon \right) |\hat{u}^m|} \, d\omega \tag{19}$$

and

$$J_{\mathrm{ph},\mathbf{u}}(\mathbf{u}) \cdot \mathbf{v} = 2 \sum_{m=1}^{3} \int_{\omega_{\min}}^{\omega_{\max}} \mathrm{Re}\left(\frac{\overline{\hat{u}^m}}{|\hat{u}^m| + \varepsilon} - \frac{\overline{\hat{u}_{\mathrm{dat}}^m}}{|\hat{u}_{\mathrm{dat}}^m| + \varepsilon} \right) \left(\frac{\hat{v}^m}{|\hat{u}^m| + \varepsilon} - \frac{\hat{u}^m}{\left(|\hat{u}^m| + \varepsilon \right)^2} \frac{\mathrm{Re}\left(\overline{\hat{u}^m}\, \hat{v}^m \right)}{|\hat{u}^m|} \right) d\omega$$

$$= 2 \sum_{m=1}^{3} \int_{\omega_{\min}}^{\omega_{\max}} \left(\frac{\mathrm{Re}\left(\hat{u}^m\, \overline{\hat{v}^m} \right)}{\left(|\hat{u}^m| + \varepsilon \right)^2} \left(1 - \frac{|\hat{u}^m|}{|\hat{u}^m| + \varepsilon} \right) - \frac{\mathrm{Re}\left(\hat{u}_{\mathrm{dat}}^m\, \overline{\hat{v}^m} \right)}{\left(|\hat{u}_{\mathrm{dat}}^m| + \varepsilon \right)\left(|\hat{u}^m| + \varepsilon \right)} + \frac{\mathrm{Re}\left(\hat{u}^m\, \overline{\hat{v}^m} \right)}{\left(|\hat{u}^m| + \varepsilon \right)^2} \frac{\mathrm{Re}\left(\overline{\hat{u}_{\mathrm{dat}}^m}\, \hat{u}^m \right)}{\left(|\hat{u}_{\mathrm{dat}}^m| + \varepsilon \right)|\hat{u}^m|} \right) d\omega$$

$$= 2 \int_{\omega_{\min}}^{\omega_{\max}} \left[\left(\frac{\varepsilon}{|\hat{u}^m| + \varepsilon} + \frac{\mathrm{Re}\left(\overline{\hat{u}_{\mathrm{dat}}^m}\, \hat{u}^m \right)}{\left(|\hat{u}_{\mathrm{dat}}^m| + \varepsilon \right)|\hat{u}^m|} \right) \frac{\mathrm{Re}\left(\hat{u}^m\, \overline{\hat{v}^m} \right)}{\left(|\hat{u}^m| + \varepsilon \right)^2} - \frac{\mathrm{Re}\left(\hat{u}_{\mathrm{dat}}^m\, \overline{\hat{v}^m} \right)}{\left(|\hat{u}_{\mathrm{dat}}^m| + \varepsilon \right)\left(|\hat{u}^m| + \varepsilon \right)} \right] d\omega. \tag{20}$$

It will turn out to be advantageous write explicitly $\overline{\hat{v}(\omega)} = \int_0^\infty e^{2\pi i \omega t}\, v(t) dt$ and exchange the order of t- and ω-integrations. With this, and the notation

$$\mathbf{g}_{\mathrm{am}}(t) = \sum_{m=1}^{3} g_{\mathrm{am}}^m(t)\, \mathbf{e}^m \tag{21}$$

with

$$g_{\mathrm{am}}^m(t) = 4 \int_{\omega_{\min}}^{\omega_{\max}} \log\left(\frac{|\hat{u}^m| + \varepsilon}{|\hat{u}_{\mathrm{dat}}^m| + \varepsilon} \right) \frac{\mathrm{Re}\left(\hat{u}^m\, e^{2\pi i \omega t} \right)}{\left(|\hat{u}^m| + \varepsilon \right) |\hat{u}^m|} \, d\omega$$

and

$$\mathbf{g}_{\mathrm{ph}}(t) = \sum_{m=1}^{3} g_{\mathrm{ph}}^m(t)\, \mathbf{e}^m$$

with

$$g_{\mathrm{ph}}^m(t) = 2 \int_{\omega_{\min}}^{\omega_{\max}} \left[\left(\frac{\varepsilon}{|\hat{u}^m| + \varepsilon} + \frac{\mathrm{Re}\left(\overline{\hat{u}_{\mathrm{dat}}^m}\, \hat{u}^m \right)}{\left(|\hat{u}_{\mathrm{dat}}^m| + \varepsilon \right)|\hat{u}^m|} \right) \frac{\mathrm{Re}\left(\hat{u}^m\, e^{2\pi i \omega t} \right)}{\left(|\hat{u}^m| + \varepsilon \right)^2} - \frac{\mathrm{Re}\left(\hat{u}_{\mathrm{dat}}^m\, e^{2\pi i \omega t} \right)}{\left(|\hat{u}_{\mathrm{dat}}^m| + \varepsilon \right)\left(|\hat{u}^m| + \varepsilon \right)} \right] d\omega \tag{22}$$

for $m = 1, 2, 3$, we get

$$\tilde{J}_{\mathrm{am},\mathbf{u}}(\mathbf{u}) \cdot \mathbf{v} = \int_0^T \mathbf{g}_{\mathrm{am}}(t) \cdot \mathbf{v}(t) \, dt \tag{23}$$

and

$$J_{\mathrm{ph},\mathbf{u}}(\mathbf{u}) \cdot \mathbf{v} = \int_0^T \mathbf{g}_{\mathrm{ph}}(t) \cdot \mathbf{v}(t) \, dt. \tag{24}$$

We now continue by introducing the adjoint system

$$M^t \mathbf{w}''(t) - D^t \mathbf{w}'(t) + A^t \mathbf{w}(t) = \mathbf{r}(t), \tag{25a}$$

$$\mathbf{w}(T) = \mathbf{w}'(T) = 0. \tag{25b}$$

The component of the right-hand side vector $\mathbf{r}$ corresponding to the test function $\boldsymbol{\varphi}_j^m$ are given by

$$\mathbf{r}_j^m(t) = N_j(\mathbf{x}_{\mathrm{out}}) \left(g_{\mathrm{am}}^m(t) + g_{\mathrm{ph}}^m(t) \right). \tag{26}$$

Note that an end-time condition $\mathbf{w}(T) = \mathbf{w}'(T) = 0$ is imposed on the adjoint equation (25). Consequently, we will have to solve (25) backward in time on the interval $[0, T]$.

Using (18), (23), and (24), we obtain

$$J_{p_\nu}(\mathbf{p}) = \int_0^T \left(\mathbf{g}_{\mathrm{am}}(t) + \mathbf{g}_{\mathrm{ph}}(t) \right) \cdot \sum_{j=1}^{N} N_j(\mathbf{x}_{\mathrm{out}})\, \mathbf{y}_{j,p_\nu}(t) \, dt = \int_0^T \left\langle \mathbf{r}(t), \mathbf{y}_{p_\nu}(t) \right\rangle dt.$$

The adjoint equation (25) further implies

$$J_{p_\nu}(\mathbf{p}) = \int_0^T \left\langle M^t \mathbf{w}''(t) - D^t \mathbf{w}'(t) + A^t \mathbf{w}(t), \mathbf{y}_{p_\nu}(t) \right\rangle dt$$

$$= \int_0^T \left(\left\langle \mathbf{w}''(t), M \mathbf{y}_{p_\nu}(t) \right\rangle - \left\langle \mathbf{w}'(t), D \mathbf{y}_{p_\nu}(t) \right\rangle + \left\langle \mathbf{w}(t), A \mathbf{y}_{p_\nu}(t) \right\rangle \right) dt.$$

After two partial integrations, using the initial and end conditions (17b) and (25b), we get

$$J_{p_\nu}(\mathbf{p}) = \int_0^T \left\langle \mathbf{w}(t), M \mathbf{y}_{p_\nu}(t)'' + D \mathbf{y}_{p_\nu}(t)' + A \mathbf{y}_{p_\nu}(t) \right\rangle dt.$$

Finally, the sensitivity equation (17a) yields

$$J_{p_\nu}(\mathbf{p}) = \int_0^T \left\langle \mathbf{w}(t), -\left(M_{p_\nu} \mathbf{y}''(t) + D_{p_\nu} \mathbf{y}'(t) + A_{p_\nu} \mathbf{y}(t) \right) \right\rangle dt$$

$$= \int_0^T \left(\left\langle \mathbf{w}'(t), M_{p_\nu} \mathbf{y}'(t) \right\rangle - \left\langle \mathbf{w}(t), D_{p_\nu} \mathbf{y}'(t) + A_{p_\nu} \mathbf{y}(t)) \right\rangle \right) dt. \tag{27}$$

For the last equality we carried out yet another partial integration in the time domain. In this final form, the sensitivity can be readily implemented because most solution algorithms for the ODEs (9) and (25) will automatically provide approximations for the solution vectors and their first time-derivatives.

5 Numerical Implementation of the Optimisation Process

In this section we explain our algorithmical approach via BFGS algorithms to find the optimal parameters w.r.t. (15). We also address the possible choices of the constants ε, $\omega_{\max}$ and $\omega_{\min}$ occuring in (15) as well as our choice for the start parameters.

5.1 Regulation of low amplitude supression

As we have seen in Section 3, the costfunctionals $J_{\mathrm{am}}(\mathbf{p})$, $J_{\mathrm{ph}}(\mathbf{p})$ contain a positive constant ε which prevents the degeneracy of the two cost terms. One needs to take special care about the choice of ε in the numerical implementation because it not only prevents degeneracy but also suppresses the low-amplitude part of the signal. To identify the parameters we have deliberately chosen a logarithmic scale for the amplitude of the signal in frequency domain because we want to match peaks in the signal over different scales of magnitude. In the very low amplitude regime, however, the logarithmic scale still gives a considerable mismatch between simulated and measured data which nonetheless contains very little information. The introduction of ε yields that the fraction $\frac{|\hat{u}_{\mathrm{out}}^m(\omega)| + \varepsilon}{|\hat{u}_{\mathrm{dat}}^m(\omega)| + \varepsilon}$ is close to one if both amplitudes $|\hat{u}_{\mathrm{dat}}^m(\omega)|$ and $|\hat{u}_{\mathrm{out}}^m(\omega)|$ are much smaller than ε and hence its logarithm is close to zero. By choosing ε appropriately we, therefore, set a soft bound below which amplitude mismatch is not considered any more in the cost functional. See Figure 6 in the next section for plots of amplitude decay over frequency for typical output signals.

Figure 3 shows a comparison of the cost integrand $\mathcal{J}_{\mathrm{am}}(\omega; \mathbf{p}, \varepsilon)$ defined in equation (16) for different values of ε over the frequency range $\omega \in [0\mathrm{Hz}, 8000\mathrm{Hz}]$. One recognises that a decrease of ε results in a decrease of the low-amplitude suppression, especially in the high frequency band width.

Thus, the choice of ε should equilibrate the level of noise suppression against the elimination of eigenfrequencies from the cost term J_{am}. For our application we identified a value of $\varepsilon = 1e - 10$ as a reasonable choice.

The maximal frequency $\omega_{\max}$ of the frequency window on which the data fit is performed plays a similar role. Because random noise on the measured data $\mathbf{u}_{\mathrm{out}}$ is mostly visible in the high-frequency region of the Fourier transformed signal, the cut-off frequency $\omega_{\max}$ eliminates high frequent noise from the data fit in the cost functional. Consequently, both ε and $\omega_{\max}$ play the role of regularisation parameters which help stabilising the identification process. Both, however, must not be chosen too strict. Otherwise necessary information is suppressed and not a available for the data inversion.
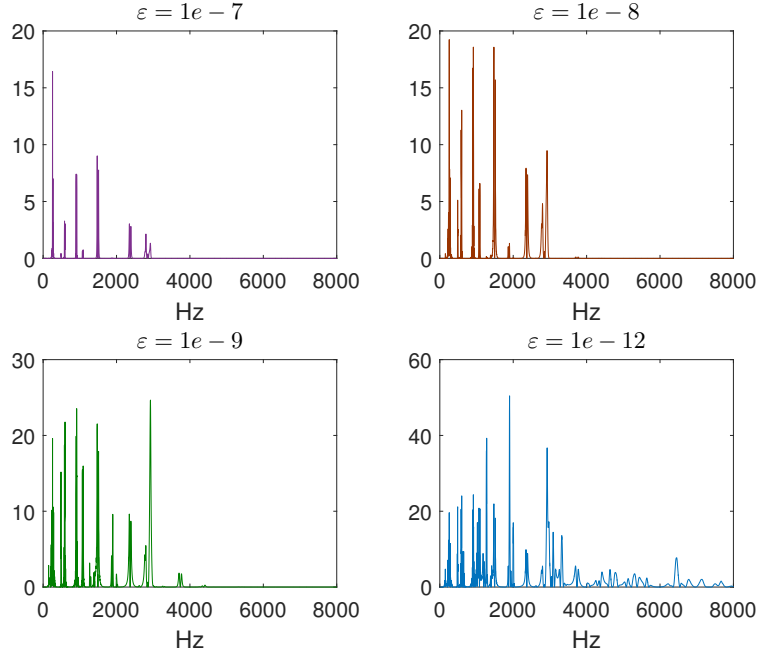
8

Figure 3: The cost integrand of $\mathcal{J}_{\mathrm{am}}(\mathbf{p}, \varepsilon)$ for different values of ε.

5.2 Choice of start parameters

A crucial point for the optimisation process is the choice of a viable start parameter set $\mathbf{p}_0$. In most cases we chose the start up parameters presented in [6, Table 3.1, Table 3.2]. Thus, usually we started with the following values for the elasticity constants displayed in Table 1. All the starting parameters are contained in the starting parameter set $\mathbf{p}_0$.

Youngs moduli	(GPa)	Shear moduli	(GPa)	Poisson Ratios	
E_1	10	G_{23}	0.29	ν_{23}	0.82
E_2	1.52	G_{13}	1.22	ν_{13}	0.5
E_3	0.87	G_{12}	1.10	ν_{12}	0.46

Table 1: Usual starting parameters for the elastic constants.

For validation purposes of the algorithmic implementation we usually generated reference output data with the parameters listed in Table 1 and started with a set of parameters $\tilde{\mathbf{p}}_0 \in \{\mathbf{p} \in \mathbb{R}^{12} : \mathbf{p}_{\mathrm{lb}} \leqslant \mathbf{p} \leqslant \mathbf{p}_{\mathrm{ub}}\}$ with given vectors $\mathbf{p}_{\mathrm{lb}} = 0.9 \cdot \mathbf{p}_0$ and $\mathbf{p}_{\mathrm{ub}} = 1.1 \cdot \mathbf{p}_0$.

5.3 Algorithmic Approach

For the optimisation we decided to implement the BFGS method from the group of quasi-Newton algorithms which only needs one gradient evaluation for each iteration step. The main motivation for the choice of the BFGS method is that it mimics the behaviour of an SQP-algorithm in the sense that it generates subproblems with balanced curveture in all directions. This is especialy advantegous in our case because our cost functional shows strongly unequilibrated behaviour in the different directions. Furthermore we have superlinear convergence for the applied approach [16]. We state the algorithmic scheme for the minimisation of J by the BFGS method like it can be found in [16], e.g.:

The step size $\alpha > 0$ for the BFGS step is computed with a line search using a local quadratic model of the cost functional. If the local model is non-convex, a backup strategy uses the last available value for the step size α. If the model is convex, the line search checks the Goldstein criteria to ensure that a reasonable descent

---

Algorithm 1 BFGS method

    Input: p_0, H_0, ε_{tol}.
    $k \leftarrow 0$;
  1: *top*:
  2: **while** $\|\nabla J_k\| > \varepsilon_{\text{tol}}$
  3: **do**
  4:     $g_k = -H_k \nabla J_k$;
  5:     $p_{k+1} = p_k + \alpha_k g_k$ (α_k computed by line search, see (28));
  6:     compute $s_k = p_{k+1} - p_k$, $y_k = \nabla J_{k+1} - \nabla J_k$;
  7:     **Hessian update:**
  8:     compute $\rho_k = \frac{1}{y_k^\top s_k}$;
  9:     $H_{k+1} = (I - \rho_k s_k y_k^\top) H_k (I - \rho_k y_k s_k^\top) + \rho_k s_k s_k^\top$;
10:     $k \leftarrow k + 1$.
11:     **goto** 1.

---

will be achieved. For an arbitrary cost functional J they read as:

$$J(p_k) + (1 - c)\alpha_k \nabla J_k^\top g_k \leqslant J(p_k + \alpha g_k) \leqslant J(p_k) + c\alpha_k \nabla J_k^\top g_k \,, \tag{28}$$

where the subscript k indicates the current values of the parameters and iterates at step k. Here g_k denotes the current search direction, p_k the current iterate and ∇J_k the gradient of J for the current iterate. The constant c in general ranges between 0 and 0.5, in our concrete application we chose $c = 0.25$. The first inequality controls the step length from below to prevent the algorithm from getting stuck in diminishing step lengths. The second inequality condition is also known as the Armijo condition and ensure a significant decrease along the search direction p_k. If it is not possible to fulfill both conditions after a fixed number n of step length increases, only the Armijo rule will be checked. If the step size also fails to fulfill the Armijo condition, we fall back to our backup strategy for the step size.

For the computation of the solutions $\mathbf{u}_{\text{out}}$ of (9) we used a Newmark-β-time-stepping scheme [12]. For a time-step size δ_t the structural equations read as

$$u_{i+1} = u_i + \delta_t \dot{u}_i + \frac{\delta_t^2}{2} \left((1 - 2\beta) \ddot{u}_i + 2\beta \ddot{u}_{i+1} \right)$$
$$\dot{u}_{i+1} = \dot{u}_i + \delta_t \left((1 - \gamma) \ddot{u}_i + \gamma \ddot{u}_{i+1} \right) \,.$$

This time-stepping scheme is unconditionally stable and second order accurate for $\beta = 1/4$ and $\gamma = 1/2$.

6   Numerical examples

We perform our numerical examples using artificial data generated by the code we use for the simulation of the elastic wave equation. For the input signal we consistently use an enforced displacement of a given point on the upper right part of the back side of the bridge in all cases. We impose a displacement in all three space dimensions where the amplitude of the displacement takes the form of a chirp signal in time. The chirp runs trough frequencies between 60 Hz and 16000 Hz and acts over a time interval of 0.08 sec. See the first plot in Figure 6 for a close-up of the first 0.015 sec of the chirp input. The total time-interval for the simulation ends usually at $T = 0.15$ sec. As output signal, we record the displacement in all three space dimensions at a measurement point $\mathbf{x}_{\text{out}}$ at the front side. Figure 6 shows the locations of input and measurement points on the bridge. The left image shows the back side, the right one, the front side. In Figure 6, plots 2–4, a typical time series for the three dimensional output signal is depicted.

In the cost functional (15), we compare simulated and measured output data in frequency space on a logarithmic scale. Figure 6 shows logarithmic plots of the amplitudes of all three space dimensions of the output signal. As expected, the amplitudes decay over the frequency range. Certain concise peaks in the signals correspond to frequencies of eigenvalues of the linear system (9). In the next Figure 6 we compare a noise-free signal to one where 5% random Gaussian noise was added to the output in time-domain. In frequency-domain, the noise takes control over the signal at a frequency of about 10000 Hz. We therefore cut off the matching
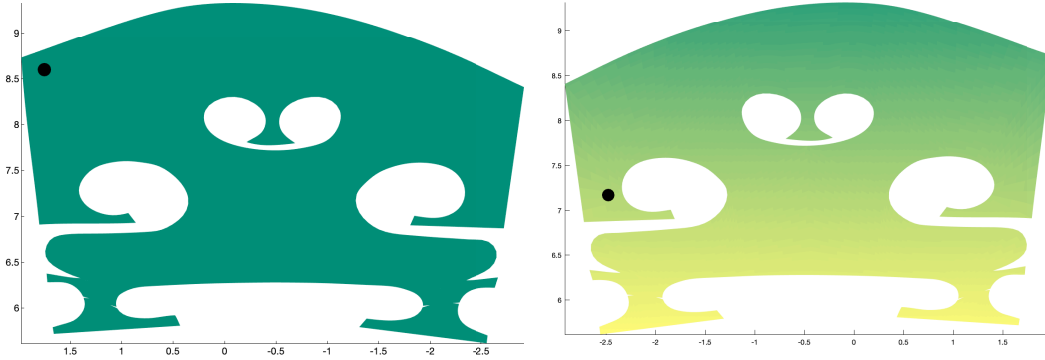
Figure 4: Location of input and output points on the bridge. Left: input location, right: output location.
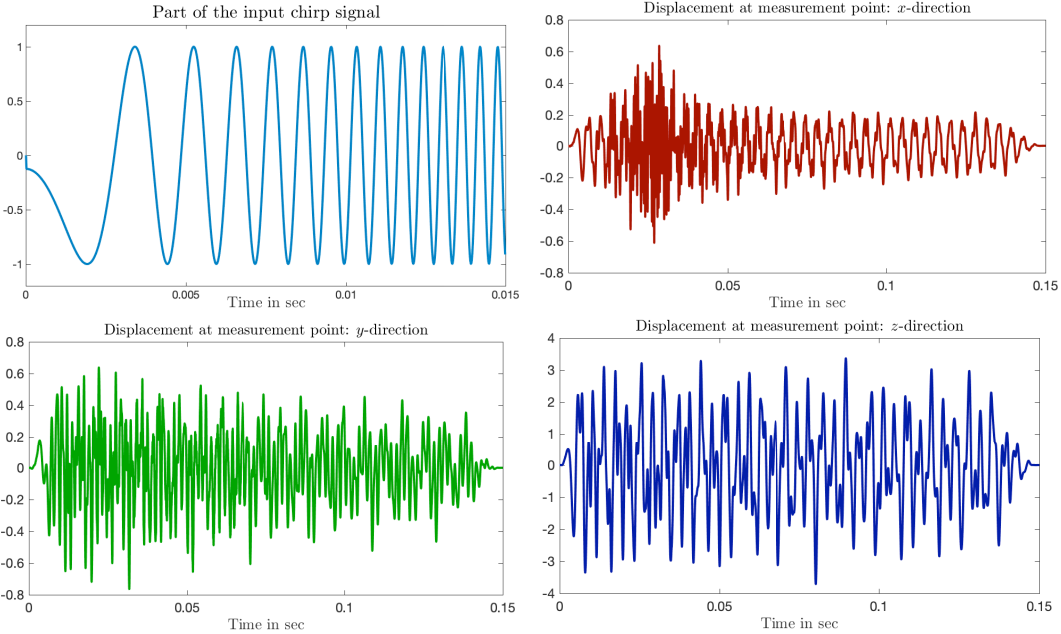

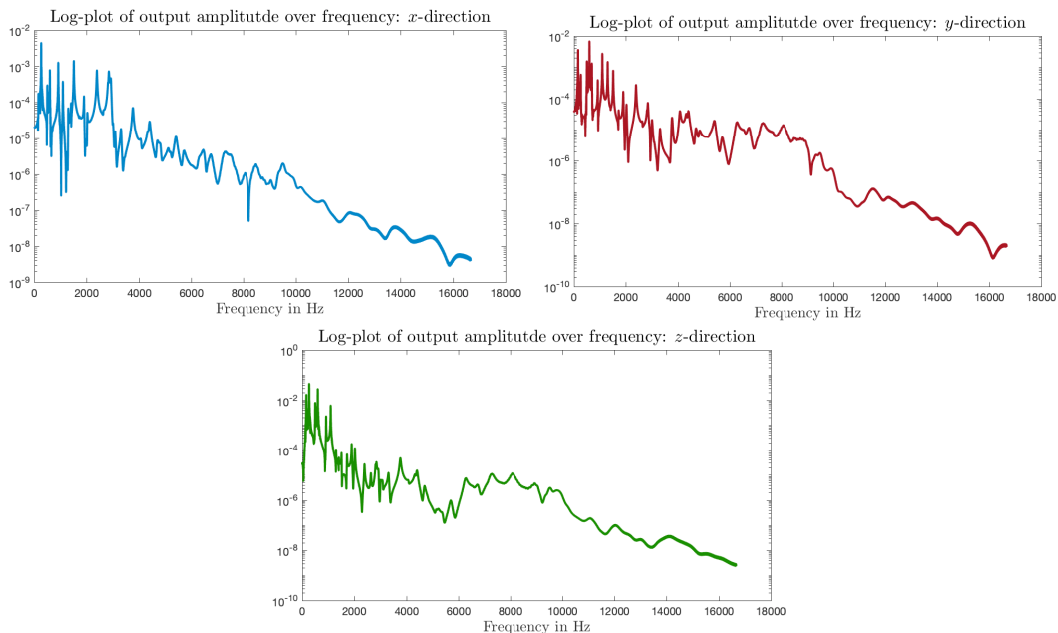Figure 5: Input and output signals for a typical simulation run.

Figure 6: Amplitude of output signal in three space dimensions over frequency. Logarithmic scale.
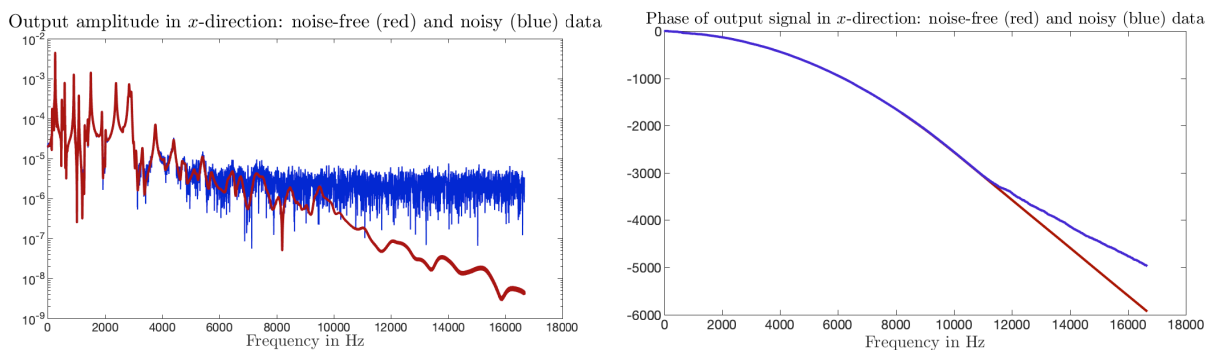

Figure 7: Amplitude and phase for noise-free and noisy (5%) data.

of simulated and given data at an upper frequency $\omega_{\max} = 10000$ Hz or even below. The lower bound for the frequency interval was set to $\omega_{\min} = 0$ Hz. The plot on the right-hand side in Figure 6 shows the phase for the noise-free and noisy signal. Both phase curves were unwrapped to create a smooth curve over the frequency range. The two curves start to diverge also at about the same frequency of 10000 Hz. Due to the data noise, (necessary) jumps of 2π are occasionally omitted in the unwrapping process for the noisy signal. Consequently, the average slope of the noisy phase is flatter than the slope of the noise-free curve in the range above 10000 Hz.

As a stopping criterion for the optimisation we usually worked with the gradient bound $\|\nabla J\| < 10^{-4}$.

Table 2 shows the reconstructed values of Young's and shear moduli for different noise-levels on the data along with the number of iterations up to termination due to the stopping criterion. For the noise-free run, we used an upper bound $\omega_{\max} = 10000$Hz whereas for the runs with noisy data, we cut off the frequency interval at $\omega_{\max} = 8000$Hz. The Poisson rations, mass density and damping parameters were set to the true reference values and not changed during the iterations.

Finally, let us examine the individual runs sumarised in Table 2 in more detail. Figure 6 shows the development of the cost functional and the norm of the gradient over the number of iterations of the optimisation algorithm, both in a semilogarithmic scale. It is evident that the cost functional repeatedly remains nearly constant over a number of iterations just to drop off steeply at the end of these platforms. This behavior indicates the strong non-convexity of the cost functional and makes the inverse problem numerically difficult and

Parameter:	true	Starting val.	Reconstructions				
Noise level:			0%	0.5%	1%	5%	10%
E_{11}	10000	9575.85429	10000.00012	9999.99985	10000.00111	9999.99933	9999.99819
E_{22}	1520	1452.20042	1519.99997	1519.99992	1520.00007	1519.99987	1519.99922
E_{33}	870	872.67939	870.0026	870.0146	869.96682	870.02698	870.16214
G_{23}	290	291.99589	290.0	289.99998	290.00008	289.99998	289.99991
G_{13}	1220	1216.26566	1220.00008	1220.00025	1219.99954	1220.00036	1220.00216
G_{12}	1100	1046.30923	1100.0	1099.99997	1100.00001	1099.99995	1099.99967
rel. error	0	0.1489	$3.117 \cdot 10^{-6}$	$4.2196 \cdot 10^{-6}$	$3.8949 \cdot 10^{-5}$	$3.154 \cdot 10^{-5}$	$1.89436 \cdot 10^{-4}$
No. of iterations	-	-	61	67	66	68	70

Table 2: Reconstructed Young's and shear moduli from noisy data sets.
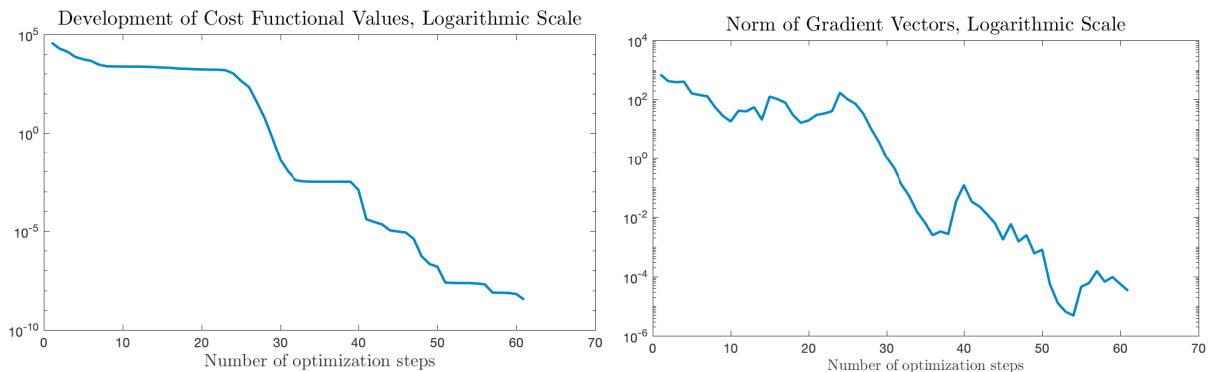
Figure 8: Development of the cost functional and gradient norm for identification of Young's and shear moduli. Noise-free data.

strongly dependent on a good choice for the initial parameter vector. The next Figure 6 shows the development of the relative errors of the reconstructed parameter over the iterations, again in a semilogarithmic scale. We see similar platforms in the errors as we see for the cost functional. It can be observed that the parameter E_{33} is not reconstructed as well as the others and that the decrease in the error for this parameter set in later than for the others. The parameter E_{33} is Young's modulus in z-direction, the direction in which the bridge has its smallest extension. It is evident from the reconstructions that the input-output relation is least sensitive with respect to the Young's modulus in this direction which makes it harder to determine.

The experiments with noisy data show that the parameter identification process is very robust with respect to data noise. The iteration numbers up to fulfillment of the stopping criterion grow only slowly with increasing noise level and the relative error is quite small even for 10% noise in the data. The qualitative behaviour shown in the plots in Figures 6–6 for 1% and 10% noise respectively changes only little with varying noise.

Table 3 and Figures 6–6 show the results for the identification of the Poisson ratios. Here the Young's and shear moduli along with the mass density and the damping parameters were held fixed at the true reference value and the optimisation was performed only with respect to the three Poisson rations. In general, the iteration numbers are less than for the identification of the 6 moduli and the reconstruction is even less sensitive to data noise. With 10% noise we still get a reconstruction with total relative error in the range of 10^{-8}. At the beginning of the optimisation the norm of the gradient is several magnitudes larger than the for the Young's and shear moduli which requires a smaller startup value for the step length in the line search.

7 Conclusion

We presented an inverse identification method for the elastic parameters of wood based on the optimisation of dynamical output data of a investigated material sample. With the illustrative example of a violin bridge we demonstrated the capability of the presented method with a numerically complex example and successfully identified the elastic parameters even under the consideration of measurement noise. In the future, it would be of interest to extend the optimisation problem to other material classes than wood offering an even broader application of the developed method to different engineering problems.
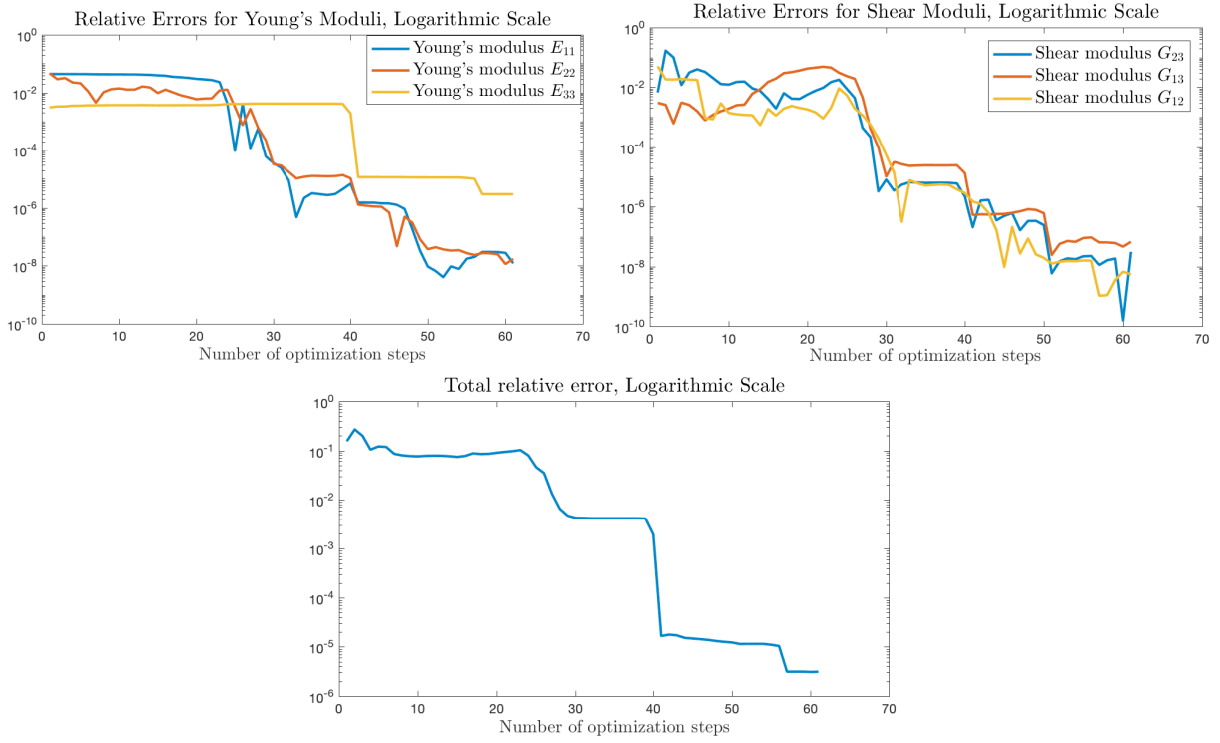
Figure 9: Development of errors for Young's and shear moduli. Noise-free data.
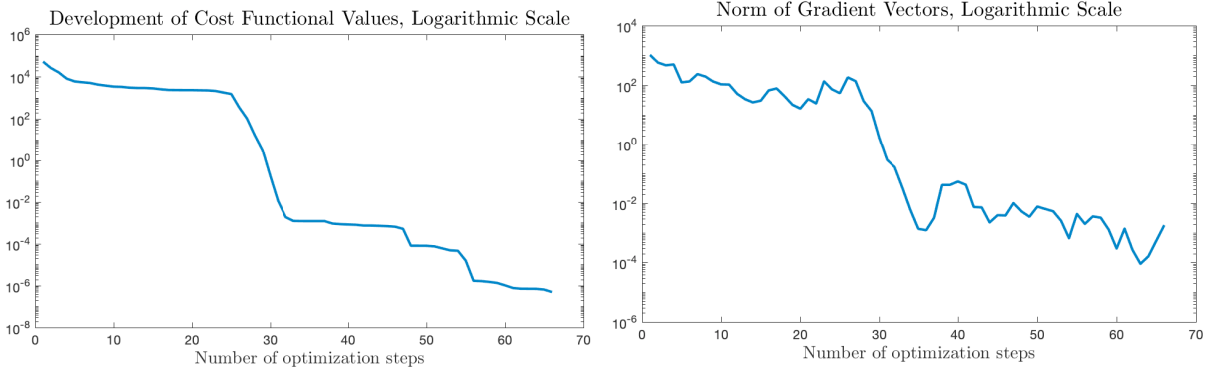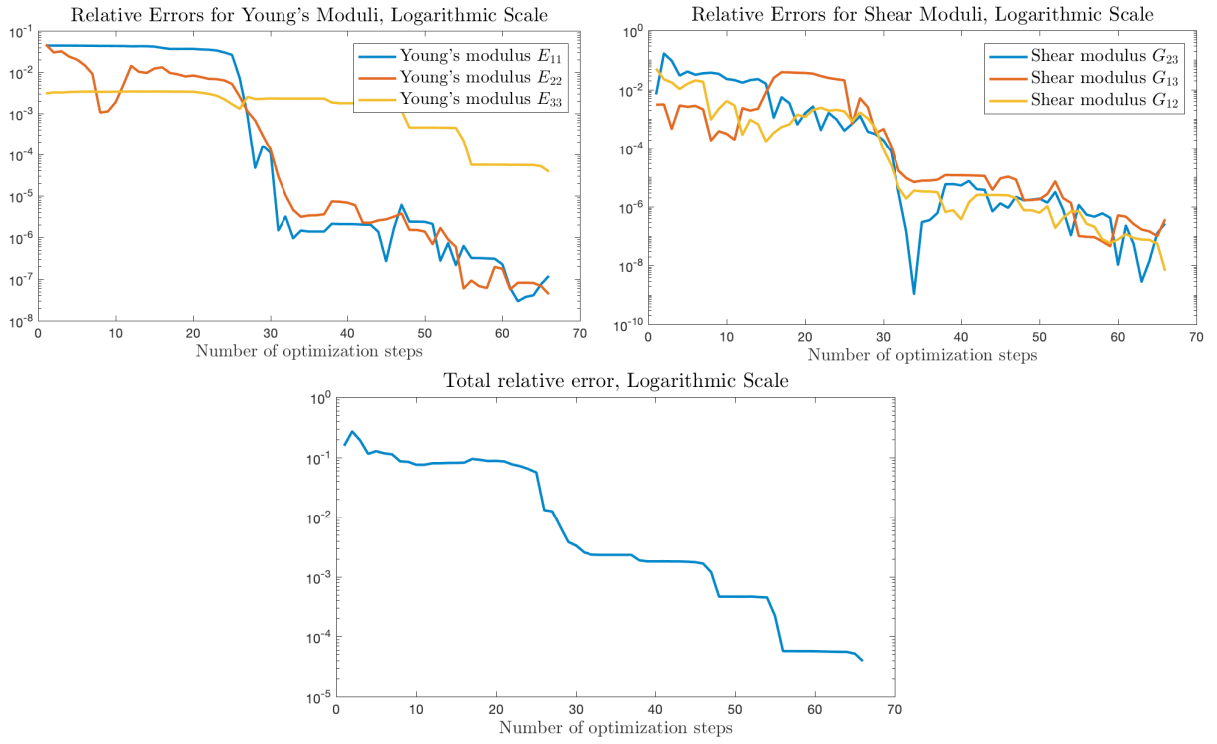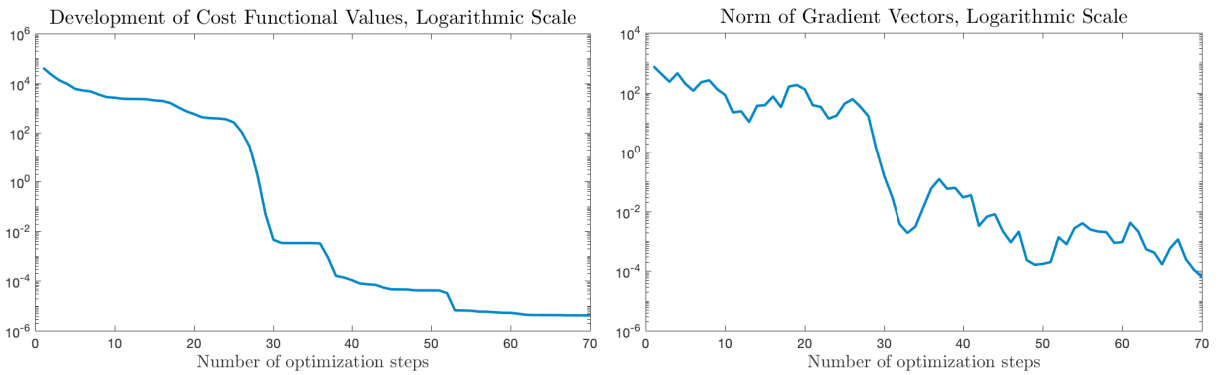

Figure 10: Development of cost functional and gradient norm for identification of Young's and shear moduli. Noise level: 1%

Parameter:	true	Starting val.	Reconstructions		
Noise level:			0%	1%	10%
ν_{21}	0.61	0.59889	0.61	0.61	0.61
ν_{32}	0.269	0.25697	0.269	0.269	0.269
ν_{31}	0.2765	0.29673	0.2765	0.2765	0.2765
rel. error	0	0.1361	$6.1519 \cdot 10^{-9}$	$6.8225 \cdot 10^{-8}$	$4.42249 \cdot 10^{-8}$
No. of iterations	-	-	16	18	19

Table 3: Reconstructed Poisson ratios from noisy data sets.

14

Figure 11: Development of errors for Young's and shear moduli. Noise level: 1%

Figure 12: Development of cost functional and gradient norm for identification of Young's and shear moduli. Noise level: 10%
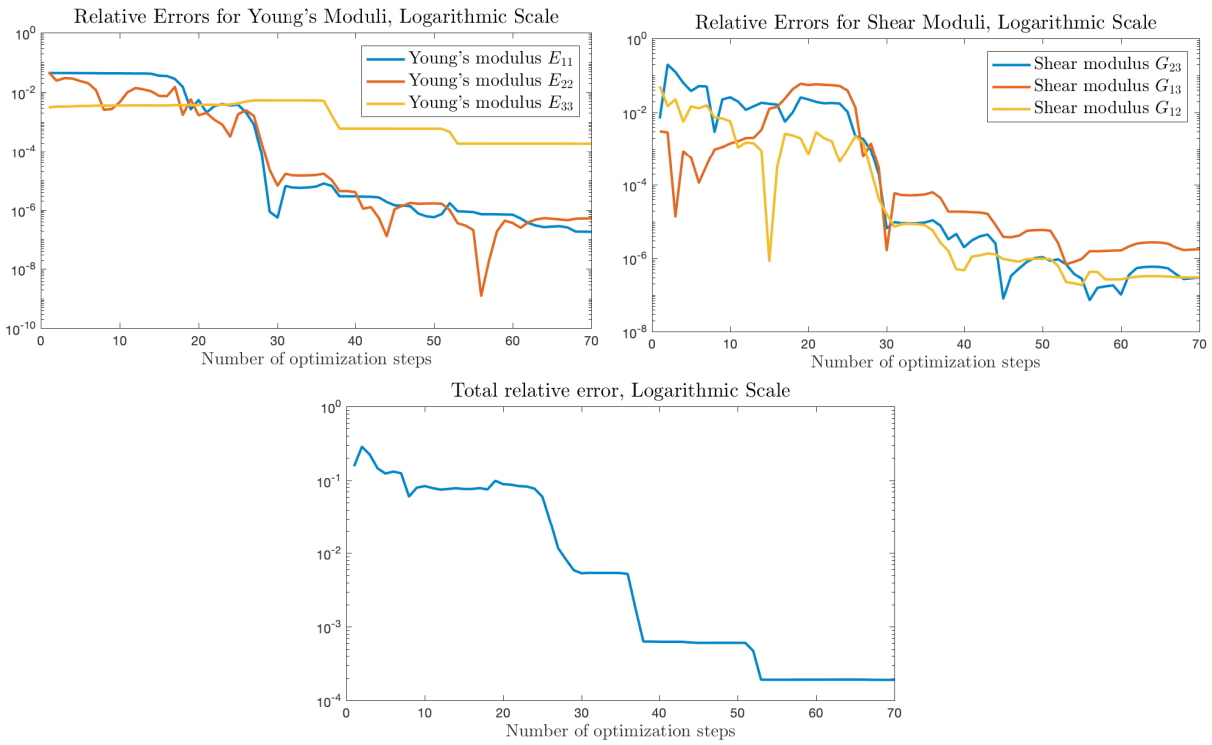
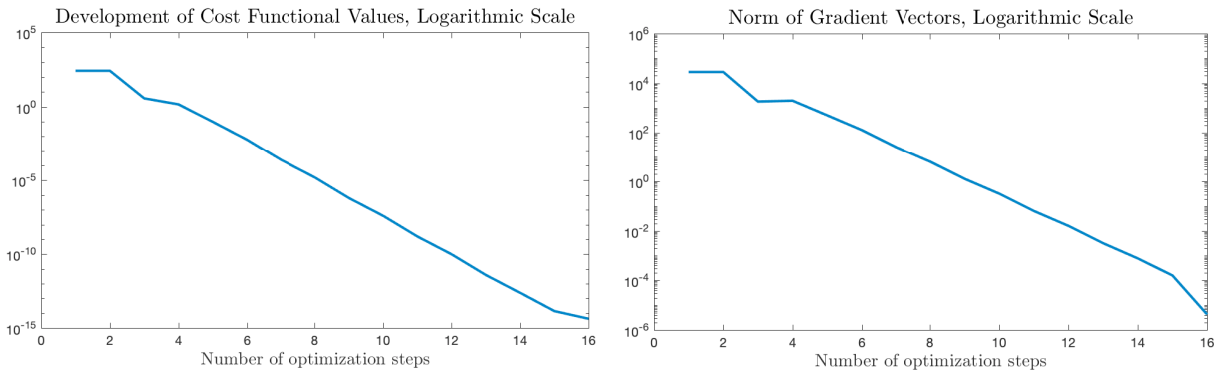Figure 13: Development of errors for Young's and shear moduli. Noise level: 10%

Figure 14: Development of cost functional and gradient norm for identification of Poisson ratios. Noise-free data
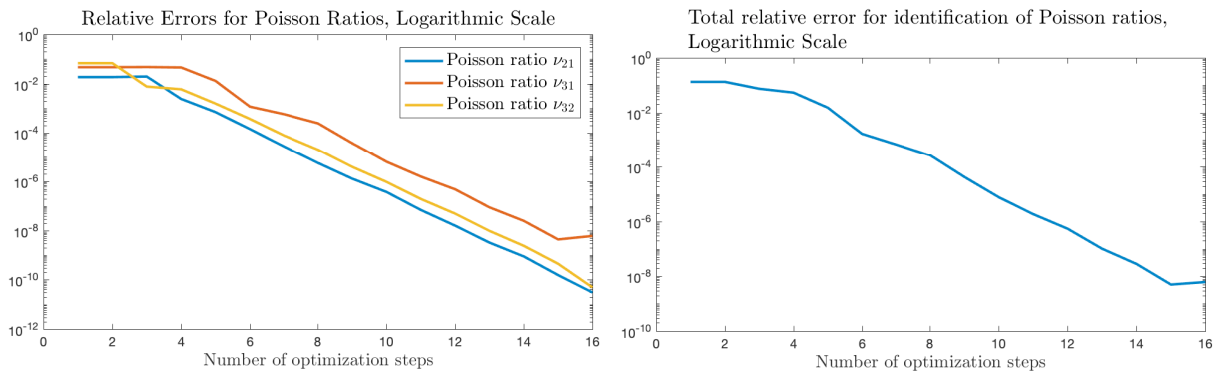

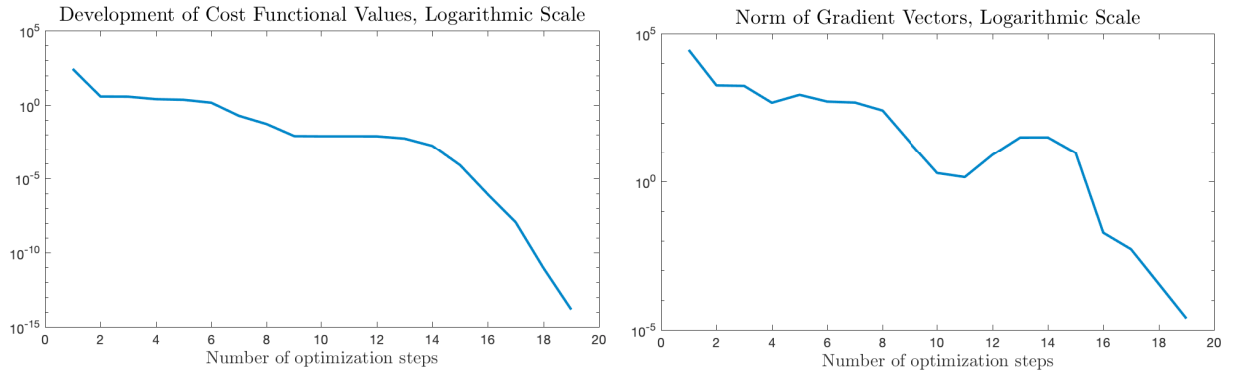Figure 15: Development of errors for Poisson ratios. Noise-free data.

Figure 16: Development of cost functional and gradient norm for identification of Poisson ratios. Noise level: 10%
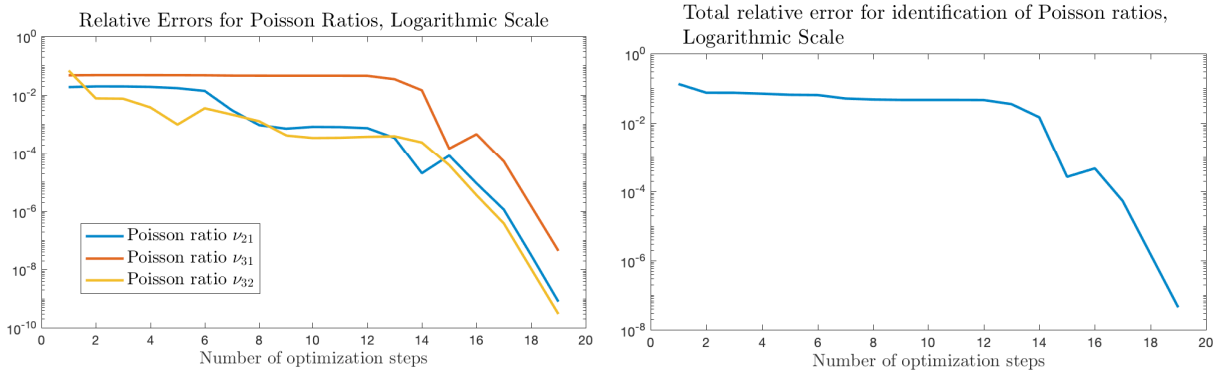

Figure 17: Development of errors for Poisson ratios. Noise level: 10%.

17

Acknowledgement

References

[1] Die Übertragungseigenschaften des streichinstrumentensteges, 1973.

[2] Herbert Amann. *Ordinary differential equations*, volume 13 of *De Gruyter Studies in Mathematics*. Walter de Gruyter & Co., Berlin, 1990. An introduction to nonlinear analysis, Translated from the German by Gerhard Metzen.

[3] Guillaume Bal, Francois Monard, and Gunther Uhlmann. Reconstruction of a fully anisotropic elasticity tensor from knowledge of displacement fields. *SIAM Journal on Applied Mathematics*, 75, 01 2015.

[4] Ericka Brivadis, Annalisa Buffa, Barbara Wohlmuth, and Linus Wunderlich. Isogeometric mortar methods. *Computer Methods in Applied Mechanics and Engineering*, 284, 07 2014.

[5] L. Bruno, F.M. Furgiuele, L. Pagnotta, and A. Poggialini. A full-field approach for the elastic characterization of anisotropic materials. *Optics and Lasers in Engineering*, 37(4):417 – 431, 2002. Optics in Italy Part I.

[6] V. Bucur. *Handbook of Materials for String Musical Instruments*. Springer International Publishing, 2016.

[7] J. Austin Cottrell, Thomas J. R. Hughes, and Yuri Bazilevs. *Isogeometric analysis*. John Wiley & Sons, Ltd., Chichester, 2009. Toward integration of CAD and FEA.

[8] L. Cremer, J.S. Allen, and MIT Press. *The Physics of the Violin*. MIT Press, 1984.

[9] E. Crossen, M.S. Gockenbach, B. Jadamba, A.A. Khan, and B. Winkler. An equation error approach for the elasticity imaging inverse problem for predicting tumor location. *Computers & Mathematics with Applications*, 67(1):122 – 135, 2014.

[10] N.H. Fletcher and T.D. Rossing. *The Physics of Musical Instruments*. Springer New York, 2013.

[11] M Hajhashemkhani, MR Hematiyan, and S Goenezen. Inverse determination of elastic constants of a hyper-elastic member with inclusions using simple displacement/length measurements. *The Journal of Strain Analysis for Engineering Design*, 53(7):529–542, 2018.

[12] Manfred Kaltenbacher. *Numerical Simulation of Mechatronic Sensors and Actuators*. Springer Verlag, Berlin–Heidelberg, second edition, 2007.

[13] David Lecompte, Arwen Smits, Hugo Sol, John Vantomme, and Danny Van Hemelrijck. Mixed numericalexperimental technique for orthotropic parameter identification using biaxial tensile tests on cruciform specimens. *International Journal of Solids and Structures*, 44(5):1643 – 1656, 2007.

[14] Hui Li, Bitao Lai, and Huihai Liu. Determination of tensile elastic parameters from brazilian tensile test: Theory and experiments. *Rock Mechanics and Rock Engineering*, 52, 02 2019.

[15] Sandra Marschke, Linus Wunderlich, Wolfgang Ring, Klaus Achterhold, and Franz Pfeiffer. An approach to construct a three-dimensional isogeometric model from μ-ct scan data with an application to the bridge of a violin. *Computer Aided Geometric Design*, 78, 2020.

[16] J. Nocedal and S. Wright. *Numerical Optimization*. Springer Series in Operations Research and Financial Engineering. Springer New York, 2006.

[17] Omri Rand and Vladimir Rovenski. *Analytical methods in anisotropic elasticity*. Birkhäuser Boston, Inc., Boston, MA, 2005. With symbolic computational tools, With 1 CD-ROM (Windows, Macintosh and UNIX).

[18] N. Saba, M. Jawaid, and M.T.H. Sultan. 1 - an overview of mechanical and physical testing of composite materials. In Mohammad Jawaid, Mohamed Thariq, and Naheed Saba, editors, *Mechanical and Physical Testing of Biocomposites, Fibre-Reinforced Composites and Hybrid Composites*, Woodhead Publishing Series in Composites Science and Engineering, pages 1 – 12. Woodhead Publishing, 2019.

[19] Abbas Samani and Donald Plewes. An inverse problem solution for measuring the elastic modulus of intactex vivobreast tissue tumours. *Physics in Medicine and Biology*, 52(5):1247–1260, jan 2007.